Monitoring Inflow Dynamics in a Multipurpose Dam Based on Travel-Time Principle

Mohamad Basel Al Sawaf
Hiroshima Daigaku - Higashihiroshima Campus: Hiroshima Daigaku
kiyosi Kawanisi (kiyosi@hiroshima-u.ac.jp)
Hiroshima Daigaku Kogakubu Daigakuin Kogaku Kenkyuka https://orcid.org/0000-0002-0070-2892
Cong Xiao
Hiroshima Daigaku - Higashihiroshima Campus: Hiroshima Daigaku
Gillang Noor
Hiroshima Kokusai Daigaku - Higashihiroshima Campus: Hiroshima Kokusai Daigaku
Faruq Khadami
Hiroshima Daigaku - Higashihiroshima Campus: Hiroshima Daigaku
Nugrahaning Gusti
Hiroshima Daigaku - Higashihiroshima Campus: Hiroshima Daigaku

Research Article

Keywords: Dam lake, Inflow, Hydroacoustics, Slow inflow velocities, Travel-time, Flow direction.

Posted Date: June 3rd, 2021

DOI: https://doi.org/10.21203/rs.3.rs-581117/v1

Monitoring inflow dynamics in a multipurpose dam based on travel-time principle

Mohamad Basel Al Sawaf [a], Kiyosi Kawanisi[*a], Cong Xiao [a], Gillang Noor [a], Nugrahaning Gusti [a], Faruq Khadami [a]

[a]Department of Civil and Environmental Engineering, Graduate School of Engineering, Hiroshima University, 1-4-1 Kagamiyama, Higashi-Hiroshima 739-8527, Japan

***Corresponding author**: kiyosi@hiroshima-u.ac.jp (K. Kawanisi); OrcID: 0000-0002-0070-2892

Abstract

Understanding inflow dynamics in a dam lake forms the basis for optimal dam operation and management practices. However, methods pertaining to adequately determining negative inflows and addressing them, as well as quantifying uncertainties in dam inflow, have been scarcely investigated. In this study, the inflow was observed using two pairs of fluvial acoustic tomography (FAT) systems placed diagonally in a dam lake, forming a crossed-shaped pattern. The "travel-time" principle is the primary approach for measuring the inflow by FAT. The novelty of this study is in discussing the inflow characteristics within a slow water-flow environment monitored by FAT. Based on the reciprocal sound transmission, we upgraded an equation to estimate the flow direction; this newly proposed generalized equation can be used in a fluctuating flow environment. We also discussed the sound propagation characteristics for slow flow velocities. Finally, we demonstrated that a small inaccuracy in the acoustic signal, even by a sub-millisecond,

23 can cause significant errors in measurements. One of the novel findings of this study is
24 the detection of internal waves using the improved flow direction equation and acoustic
25 travel-time records. Overall, this study presents a promising approach for inflow
26 measurements under extremely slow flow conditions.

27

28 **Keywords**: Dam lake, Inflow, Hydroacoustics, Slow inflow velocities, Travel-time, Flow
29 direction.

1. Introduction

Dams are important hydraulic structures because they have various positive impacts on the environment (Hariri-Ardebili 2018) through single or multi-purpose functions, including flood control, water supply, and hydroelectric power generation. However, dam construction is accompanied by the transformation of a wide range of aquatic ecosystems and alteration of river flow dynamics. Among the most prominent effects of dam construction are variations in sediment transport conditions, alteration of river thermal regime, obstruction of fish migratory patterns, and destabilization of riverine biodiversity (Allan 2004; Nazeer et al. 2016; Stähly et al. 2019). These effects may continue for many years, even decades, or constitute a permanent ecohydrological change that may or may not reach a new equilibrium. Hence, understanding the effects of a dam on upstream and downstream sites is a key challenge in ecohydrology (Gupta et al. 2012).

Accurate measurement of dam inflow is critical because it allows for optimal planning and management practices with respect to water resources, particularly for flood control and power generation. Control strategies for power generation vary for low and high inflow rates. Similarly, dam flush patterns are scheduled and calibrated based on the recorded amount of inflow, which differs during dry and rainy days (Ahmad and Hossain 2019). Accurate dam inflow forecasting has been a focal point in recent research studies (Ahmad and Hossain 2019; Hadiyan et al. 2020). The selection of suitable methods for accurate inflow forecasting and modeling considerably depends on watershed characteristics and available data. In this regard, accurate real-time and/or quasi real-time quantification of stream dynamics is a severe challenge encountered while improving the

performance of reservoir inflow forecasting, creating physical models of dam inflow, and, more importantly, regulating the outflow quantities.

Typically, dam inflow is computed using the main water balance method represented by the following equation:

$$Q_I = Q_O + \frac{\Delta S}{\Delta T} + Q_L \quad (1)$$

where Q_I and Q_O are the reservoir inflow and outflow, respectively; ΔS ($\Delta S = S_{i+1} - S_i$) is the difference between the final and initial water storage for the time period ΔT ($\Delta T = T_{i+1} - T_i$); and Q_L is the amount of water loss from the reservoir, including that from evaporation and seepage (Deng et al. 2015). The temporal variation in the reservoir storage, S_i, is a function of the observed water level, H_i, and can be expressed as $S_i = f(H_i)$. Nonetheless, uncertainties exist in the reservoir inflow derived by the main water balance method as a result of errors in the reservoir stage-storage relationships and water level measurements (Tao 1999). Stage-storage errors are generated by continuous alteration in the topography of the reservoir lake due to continuous sediment deposition mobilized from upstream regions and as a consequence of poor lake bed and terrain surveying techniques. The limitations of water level monitoring techniques, along with certain natural influencing factors, such as reservoir waves, induce errors in the water level records (Deng et al. 2015).

Previous studies aimed to improve reservoir inflow measurements and minimize potential errors in the inflow estimates using various approaches, such as the ensemble Kalman filter (EnKF) (Deng et al. 2015), applying the moving average of mean water balance equation (Budu 2014), and employing remote sensing information for reservoir slope

storage computation (Suzuki et al. 2008). These studies have led to improvements in the accuracy of dam inflow quantification; however, additional efforts should be directed toward improving the precision of reservoir inflow measurement techniques. Likewise, certain issues related to dam inflow estimation, such as adopting methods to accurately address and determine the negative inflows and quantify the uncertainties in dam inflow, have received little attention.

In cases of considerably slow flow environments, such as inflow to a dam lake, measuring variations in water stage and storage does not reflect sufficient precise information on real-time inflow dynamics. Alternatively, to acquire an average stream cross-sectional velocity and the corresponding flowrate, a set of one-point current meters can be installed. However, this approach cannot be considered practical for long-term measurement in sites such as dam lakes and may even be obstructed in certain locations due to site utilization by fisheries or shipping traffic (Zhu et al. 2012).

This study presents findings from a site-based observation of the inflow to a dam lake obtained using an advanced hydroacoustic tomography system; this study is based on travel-time principles and discusses the prominent issues observed during our monitoring program. We aim to answer the following research questions: 1) What kind of information and knowledge can be derived using underwater acoustic tomography during the slow flow of controlled reservoir releases? 2) What kind of hydrological processes can be identified to improve and correct the analytical models for inflow estimation? Our main objective was to identify the hydrological features that can be deduced from sound transmission in water within slow flows, rather than developing advanced analytical models to calculate the accurate inflow values.

97 The key contributions of this study are novel in different aspects. First, to the best of our
98 knowledge, in a scientific sense, cross-sectional average velocity and inflow
99 measurements in a shallow dam lake (by means of reciprocal sound transmission) have
100 not been investigated previously. In this study, we observed the temporal variations of
101 inflow dynamics using crossed acoustic path configurations executed by two pairs of
102 hydroacoustic tomographic systems with two distinct frequencies, which also offers a
103 technical novelty to our study. Moreover, we upgraded the determination of flow
104 direction proposed in a previous study by improving it to determine fluctuating flow
105 direction. The greatest advantages of hydroacoustics are its speed, functionality, and
106 accuracy in providing a detailed image, thereby facilitating a reliable understanding of
107 the hydrological processes that otherwise could not be identified by conventional means
108 of hydrological systems analysis.

109 The remainder of this paper is organized as follows. The study area of Haji Dam and
110 Yachiyo Lake and the methods used in our study are described in Section 2. The results
111 and discussion are presented in Sections 3 and 4, respectively. Finally, the main
112 conclusions are presented in Section 5.

113 ## 2. Materials and methods

114 *2.1. Study area*

115 Field observations were conducted in Haji Dam, a concrete gravity dam located in
116 Akitakata City, Hiroshima, Japan (Fig. 1). Haji Dam was built on the upstream region of
117 the Gōno River, which is the main river in Chūgoku area (Hiroshima, Okayama, Shimane,
118 Tottori, and Yamaguchi.). Its mainstream rises from the mountain region of the

Kitahiroshima city, runs through Hiroshima and Shimane prefectures, and finally, discharges into the Sea of Japan near Gōtsu town in Shimane prefecture (Fig. 1a). The climate of the dam region is generally warm and temperate. The mean annual temperature is 11.7 °C, and the annual precipitation is approximately 1800 mm.

Table 1. Main specifications of Haji dam and its storage lake (Yachiyo Lake)

Haji Dam specifications	
Dam wall height	50 m
Dam wall top length	300 m
Dam mass	210,000 m^3
Catchment area	307.5 km^2
Yachiyo Lake area	2.8 km^2
Full reservoir storage capacity	47,300,000 m^3
Effective water storage capacity	41,100,000 m^3

Table 1 lists the main characteristics of Haji Dam. The dam serves multiple purposes, including flood control (specifically during the East Asian rainy season), power generation, water supply, and irrigation, in Hiroshima prefecture. The lake formed by Haji Dam is called Yachiyo Lake. As seen in Fig. 1b, the dam lake is stomach-shaped, thus being an ideal area to monitor slow inflow dynamics and study several hydrological characteristics.

Fig. 1 a) Location of the observation site; b) map showing Gōno River, Haji Dam, and Yachiyo Lake; and c) study area map with inflow measurement zone and instrument positions.

2.2. Methods

135 2.2.1. Inflow measurements using fluvial acoustic tomography (FAT) system

136 In this study, tomographic measurements of inflow at Yachiyo Lake were performed
137 using a fluvial acoustic tomography (FAT) system. Based on the travel-time approach,
138 the FAT system is capable of computing the cross-sectional average sound speed in water
139 (c) and flow velocity along the sound ray path (u). Travel time is the time it takes to
140 transmit an acoustic pulse from one transducer to the target transducer. Hence, for a pair
141 of transducers (such as S1 and S2; Fig. 1c), the recorded travel times, t_{S1} (i.e., the
142 transmitted acoustic signal from upstream transducer S1 to the corresponding
143 downstream transducer S2) and t_{S2} (i.e., the transmitted acoustic signal from the
144 downstream transducer S2 to the corresponding upstream transducer S1), are used to
145 estimate the cross-sectional average sound speed and velocity along the transmission line
146 (S1_S2) as follows:

147 $$c = \frac{D_S}{2}\left(\frac{1}{t_{S1}} + \frac{1}{t_{S2}}\right) \quad (2)$$

148 $$u = \frac{D_S}{2}\left(\frac{1}{t_{S1}} - \frac{1}{t_{S2}}\right), \quad (3)$$

149 where D_S is the oblique distance between transducers S1 and S2. Accordingly, the inflow
150 using FAT can be estimated as:

151 $$Q_{FAT} = u_S \times A_S \times \tan\theta_1 \quad (4)$$

152 A_S is the cross-sectional area along transmission line S1_S2, and θ_1 is the angle between
153 transmission line S1_S2 and the inflow direction. Although several approaches can be
154 used to estimate the flow direction of the FAT system (Al Sawaf et al. 2020), we used
155 two crossed-path configuration approaches to estimate the flow direction.

A dam lake is an ideal area for analyzing sound transmission; however, to overcome obstacles encountered with sound propagation in water and attain precise data recording, the acoustic carrier signal is modulated using a maximum-length sequence (M-sequence), and the received signal is considered to be a set of multipath signals with the same arrival time. Hence, selecting the cross-correlation of the received signal with a replica of the transmitted signal is similar to sending a single strong pulse. The M-sequence is a type of pseudorandom signal, by which the phase shift of π in the carrier is produced at varying time intervals (Simon MK, Omura JK 1985).

The FAT system consists of a pair of processing units connected to underwater acoustic transducers. The main operation settings of the FAT systems used in this experiment are summarized in Table 2. In this study, two pairs of FAT systems were placed diagonally on the lake banks, forming a cross-shaped pattern, as shown in Fig. 1c. Figure 1c also shows the placements of the FAT transducers during the observation period. In this study, two different transmission frequencies were used to monitor the inflow dynamics, with different transmission rates. Along S1_S2, the transmission frequency was 53 kHz with a transmission rate of 10 s, whereas T1_T2 was accomplished using a 30 kHz transmission frequency at a transmission rate of 30 s, and both transducers served the dual function of transmitting and receiving acoustic signals.

At the beginning of the observation period, the water in the dam lake was deep; thus, all transducers were installed approximately 1.5 m below the water surface and suspended on floating boats. The floating boats were poised using nearby trees and/or rocks. At the end of each transducer, a counterweight was fixed to prevent the transducer from drifting in the event of unexpectedly high inflow velocities.

179 **Table 2.** Main operation settings of fluvial acoustic tomography systems

Station	Transmission frequency	Transducer type	Signal transmission rate	Length between stations	Expected arrival time* (milliseconds)
S1_S2	53 kHz	Omnidirectional broadband transducers (T226, Neptune Sonar Ltd)	Each 10 s	253.04 m	174.5 ms
T1_T2	30 kHz	Omnidirectional broadband transducers (T257, Neptune Sonar Ltd)	Each 30 s	287.50 m	198.2 ms

180 *Assuming that the sound speed in freshwater environment is 1450 m/s

181 There are several reasons for using two distinctive frequencies. First, a new generation of
182 the FAT system was developed in our laboratory; therefore, to assess the performance of
183 this version within slow inflow velocities, two central frequencies were tested. Second,
184 based on our experience with hydroacoustic tomography in rivers, we hypothesize that a
185 higher transmission frequency can perform outstandingly in cases of slow water velocity.
186 In addition, shorter acoustic paths (e.g., S1_S2) entail higher frequencies and vice versa.
187 Furthermore, we used a cross-shaped acoustic path to determine the continuous
188 measurements of the inflow direction (θ_1 and θ_2), as depicted in Fig. 2. This monitoring
189 pattern would be beneficial for tracking slow and fluctuating inflow directions and
190 detecting any period of negative inflows that could be encountered during the discrete
191 opening and closing of the dam gate. Additional details regarding the flow angle
192 estimation are provided in Section 2.2.2.

193 2.2.2. Determination of the inflow direction acquired using cross-shaped acoustic path
194 configuration
195 Bahreinimotlagh et al. (2016) proposed the following equation for determining flow
196 direction:

197 $$Q_{S1S2} = Q_{T1T2}, \quad (5)$$

198 $$u_1 \times A_1 \times \tan\theta_1 = u_2 \times A_2 \times \tan\theta_2 \quad (6)$$

199 where Q_{S1S2}, u_1, and A_1 are the discharge, velocity, and cross-sectional area along S1_S2,
200 respectively; Q_{T1T2}, u_2, and A_2 are the discharge, velocity, and cross-sectional area along
201 T1_T2, respectively; and θ_2 is the angle between transmission line T1_T2 and the inflow
202 direction. As illustrated in Fig. 1c, $\emptyset_1 = \theta_1 + \theta_2$ is the angle formed by the transection
203 of the two acoustic paths; therefore, it is substituted in Eq. (6) as follows:

204 $$\theta_1 = \tan^{-1}\left(\frac{u_1 \times A_1}{u_2 \times A_2} \times \tan(\emptyset_1 - \theta_1)\right) \quad (7)$$

205 In essence, θ_1 requires an iteration-solving approach; therefore, using trigonometric
206 expansion, Eq. (7) can be explicitly expressed as follows:

207 $$\theta_1 = \cos^{-1}\left(\frac{1}{2}\sqrt{\frac{\sqrt{2}\cos(\emptyset_1)\sqrt{{u_1}^2 {A_1}^2 + \cos(2\emptyset_1)(u_1 A_1 - u_2 A_2)^2 + 6 A_1 A_2 u_1 u_2 + {u_2}^2 {A_2}^2 + \cos(2\emptyset_1)(u_2 A_2 - u_1 A_1) + 3u_1 A_1 + u_2 A_2}}{u_1 A_1 + u_2 A_2}}\right) \quad (8)$$

208 Equation (8) is limited to unidirectional flow from upstream to downstream.
209 Consequently, to improve the equation representability, $\emptyset_1$ or $\emptyset_2$ must be carefully
210 selected based on the flow direction. This can be accomplished by considering the

211 difference between the arrival times of each pair of transducers and selecting proper
212 geometrical axes, as illustrated in Fig. 2. In the case of Fig. 2d, both velocities along
213 S1_S2 and T1_T2 were positive; therefore, according to Eq. (3), in this case $t_{S1} < t_{S2}$,
214 $t_{T1} < t_{T2}$ and $\emptyset_1 = \theta_1 + \theta_2$. Thus, the current direction can be inferred to be in the 4th
215 quadrant (Q4) of the x shape. Likewise, if $t_{S1} > t_{S2}$and $t_{T1} > t_{T2}$, $\emptyset_1 = \theta_1 + \theta_2$, but in
216 this case, both velocities were negative (Fig. 2b), and the direction was in the 2nd quadrant
217 (Q2). However, if $t_{S1} > t_{S2}$ and $t_{T1} < t_{T2}$ (i.e., Q1) or $t_{S1} < t_{S2}$ and $t_{T1} > t_{T2}$ (Q3),
218 then $\emptyset_2 = \theta_1 + \theta_2$ (Figs. 2a, 2c).

219

220 **Fig. 2** Visualization of flow direction over proposed axes
221 according to recorded arrival times
222

223 *2.3. Auxiliary measurements*

224 The temporal variations in the mean water level and water temperature were acquired
225 every 5 min using a HOBO®_U20 level-temperature logger attached to the bridge
226 column (see "WL" Fig. 1c). The bed topography survey along the two cross-sections
227 (S1_S2 and T1_T2) was conducted using an autonomous boat equipped with GPS and a
228 single-beam echo sounder at a frequency of 200 kHz (resolution of 0.01 m). The time
229 series of the cross-sectional area along S1_S2 and T1_T2 were evaluated by computing
230 the integration between the riverbed and the time series of the average water level
231 observed by the water level logger.

232 Water temperature profiles were collected using CastAway [a conductivity-temperature-
233 depth (CTD) logger] at different locations in the lake (P1, P2, P3, and P4 in Fig. 1c) on
234 October 19, 2020 (fall) and December 2, 2020 (early winter).

235 Finally, the records of water level, storage, inflow, and outflow were provided by the Haji
236 Dam Monitoring Office (HDMO) and used for further analyses and comparisons. The
237 inflow at Haji Dam was measured using the main water balance approach, where the
238 water level was measured continuously every 10 min using a quartz-type water-level
239 gauge monitoring unit.

240 Our observation started on November 18, 2020 and ended on December 5, 2020. Owing
241 to certain difficulties related to site accessibility due to severe climate and the restrictions
242 influenced by the COVID-19 pandemic, certain tomographic records could not be
243 obtained before November 30, 2020. No rainfall was observed during the study period.

244 ## 3. Results

245 ### *3.1. Time series of water level, storage, and water temperature during the*
246 *observation period*

247 The temporal variation at the water stage, as measured by the HDMO, is plotted in Fig.
248 3a and was consistent with the readings obtained by the water level-temperature logger.
249 In general, both water level records are highly comparable to each other, even though the
250 HDMO dataset resolution was 10 min, while the water level logger was set to 5 min.
251 Figure 3a shows that the water stage at the dam lake exhibited a daily steady increment
252 estimated at 8 cm. Nonetheless, HDMO performs a scheduled water release for 5 h every
253 afternoon, resulting in approximately 0.5% storage reduction per day (Fig. 3b).

Fig. 3 Time series plots of a) mean water level recorded by Haji Dam Monitoring Office (HDMO; red) and water level-temperature sensor (black), b) temporal variation of storage, and c) average water temperature. Releasing periods are shaded in blue

The water temperature recorded by the water level temperature logger is presented in Fig. 3c. Notably, water temperature was almost constant during the study period. As seen in Fig. 3c, the water temperature during the observation period was ~12 ℃; however, on the last day, the water temperature dropped drastically because water storage near the sensor was low.

3.2. Hydroacoustic measurements

3.2.1. Arrival time records

As depicted in Figs. 4a and b and Figs. 5a and b, samples of the stack plots for the cross-correlation pattern signals were transmitted from the downstream transducer to the upstream transducer and vice versa for S1_S2 and T1_T2, respectively. The diagrams are shown at 5 min intervals and two main groups of arrival times, with a difference of approximately 0.35 ms for the 53-kHz system. However, in the case of the 30-kHz system, only one primary arrival group is observed, whereas multiple arrival peaks are evident in Fig. 5b, with an approximate difference of 1 ms.

In this study, the first arrival peak from each cross-correlation signal was selected, and the corresponding arrival times for the downstream (i.e., t_{S2} and t_{T2}) and upstream transducers (i.e., t_{S1} and t_{T1}) are identified in Figs. 4c, 5c, 4d, and 5d, respectively, to compute the velocity and water inflow. The discontinuities in the arrival time series data indicate that these readings could not be selected because the recorded signal was

277 extremely weak. In other words, either the largest peak of each correlated signal did not
278 satisfy an acceptable signal-to-noise-ratio (SNR) threshold (10 dB), or it was
279 considerably scattered, and therefore, the arrival peak could not be defined accurately.

280 **Fig. 4** Arrival time records of 53-kHz system: sample of stack diagram of correlated
281 signals recorded on December 1, 2020, with a 5-min interval, (a) blue dots are the
282 selected peaks of the arrival times downstream and (b) red dots are the selected peaks of
283 the arrival times upstream. Time series plots of arrival times (in ms) obtained by (c) the
284 downstream (black) and (d) upstream (gray) transducers

285 **Fig. 5** Arrival time records of 30-kHz system: sample of stack diagram of correlated
286 signals recorded on December 1, 2020, with a 5-min interval, (a) blue dots represent
287 selected peaks of arrival times downstream, and (b) red dots represent selected peaks of
288 arrival times upstream. Time series plots of arrival times (in ms) obtained by (c)
289 downstream (black) and (d) upstream (gray) transducers

290

291 Remarkably, the recorded arrival times in Figs. 4c–d, and Figs. 5c–d ranged within the
292 expected values presented in Table 2. The arrival times fluctuated during the day and
293 night because of daily temperature variations. Once the arrival time records were defined,
294 the water velocity, flow direction, and inflow by FAT were calculated using Eqs. (2) and
295 (8).

296 3.2.2. Inflow velocity

297 The velocity resolution (u_r) of the FAT can be estimated using Eq. (9) (also see Fig. 6):

298 $$u_r = \frac{c_m^2}{4 \times R \times f} \qquad (9)$$

where f is the transducer frequency, R is the ray length (m), and c_m = 1450 m/s. Figure 6 demonstrates that the velocity resolution obtained by 53 kHz is 1.5 times greater than the velocity obtained by the 30-kHz transducer (in the case of our transmission lengths). In the present study, the velocity resolution acquired by f = 53 kHz (approximate ray length along S1_S2 = 253.04 m) and f = 30 kHz (approximate ray length along T1_T2 = 287.5 m) is 0.039 m/s and 0.06 m/s, respectively.

Fig. 6. Velocity resolution of fluvial acoustic tomography (FAT) as a function of acoustic ray length and transducer frequency; green and red dots denote velocity resolution in accordance with distance and frequency for S1_S2 and T1_T2, respectively

Kawanisi et al. (2012) revealed that the reliability of the FAT records increases as the square root of the number of samples per ensemble increases. Hence, to decrease the uncertainty of the FAT records, 60 samples in the case of 53 kHz (owing to the high transmission rate, i.e., 10 s individually) and 30 samples in the case of 30 kHz were averaged in this study. Consequently, the uncertainty caused by the low velocity resolution could be reduced to $\frac{0.04}{\sqrt{60}}$=0.5 cm/s and $\frac{0.06}{\sqrt{30}}$ =1 cm/s for 53 kHz and 30 kHz, respectively.

Figures 7a and 7b show the temporal variations in the cross-sectional mean velocities along S1_S2 and T1_T2, respectively. The cross-sectional average velocity along S1_S2 was evidently very slow during the investigation period, with apparent positive and negative fluctuations. Gaps in the velocity time series were generated because the original arrival times were not recorded or were unreliable.

Fig. 7 Mean average velocity along transmission lines: (a) S1_S2 (black), and (b) T1_T2 (red). Releasing periods are highlighted in blue

Similarly, the cross-sectional average velocity along T1_T2 was nearly constant, with positive and negative fluctuations observed until the late morning of December 2, 2020. However, the velocity became completely positive from the afternoon of the same day along T1_T2 and S1_S2, which was expected because of the continuous water release compared to the lower inflow rate. In fact, post December 4, 2020, the water level at the dam lake had declined significantly near the left bank, particularly at T2, as illustrated in the cross-sectional profile shown in Fig. 10b; therefore, the transducer and floating boat remained almost dried on the bank, and consequently, reliable reciprocal sound transmission along T1_T2 could not be accomplished afterwards. At midday on December 2, 2020, the velocity was not determined because the battery voltages at T1 and S2 dropped and were replaced. The velocity data were processed using the mean filter technique. This technique involves removing local variations caused by rough readings and minimizing noise levels. To evaluate the mean filter of a dataset, every point is replaced by the mean value in its range (*r)* neighborhood. Hence, in the case of the velocity obtained by the 53 and 30-kHz datasets, 60 and 30 points were used during the filtering process, respectively.

3.3.Detection of flow direction and inflow estimation by fluvial acoustic tomography (FAT)

Owing to the difference in the velocity resolutions, only the computed flow direction and inflow of optimal data records are shown. The water flow direction was computed according to the main assumptions proposed in Section 3.2 and illustrated in Fig. 2.

Figure 8a presents the temporal variations in the ensemble-averaged inflow direction between November 30, 2020 and December 1, 2020. In this figure, the flow direction across S1_S2 is marked with four colors. These colors indicate the water direction over a corresponding quadrant, according to the assumptions given in Section 2.2.2. Overall, the absolute mean flow direction was 21.47°, and this value varied in different directions. The findings in Fig. 8a reveal that the water direction mainly varied between Q1 and Q2.

Fig. 8 Time series plots of a) water flow (inflow) direction according to its corresponding quadrant, b) inflow estimated by fluvial acoustic tomography (FAT) (black) and by HDMO (red), and outflow acquired by Haji Dam Monitoring Office (HDMO; blue), and c) inflow by acquired by FAT using the mean flow direction θ = 21.47° (black) and by HDMO (red), and outflow by HDMO (blue); Releasing period is highlighted in blue

Figure 8b shows the temporal variations in the inflow acquired by FAT estimated from Eq. (4) compared to those estimated by the HDMO. The inflow estimated by FAT and that recorded by the HDMO on December 30, 2020 during release and very low release conditions are moderately comparable with each other, with considerable variations in a few periods. The large inconsistencies between FAT and HDMO estimates can be attributed to the low resolution of velocity estimates by FAT (specifically for 30 kHz), which decreased the accuracy of angle determination, or due to uncertainties in the stage-storage term in the main water balance method for inflow calculation. Another possible reason is the limitation of acoustic records in accurately determining the flow direction under slow flow conditions, particularly during the transition of the water direction from one quadrant to another.

Alternatively, considering the absolute mean value of the inflow direction as a fixed value for inflow estimation using FAT (i.e., $\theta_1 = 21.47°$), the inflow rate estimated by FAT is highly comparable to that reported by the HDMO, as depicted in Fig. 8c.

3.4. Lake thermal stratification

Thermal stratification is among the most important hydrological processes in lake hydrodynamics. Figures 9a and 9b show the temperature along the water columns measured at P1 to P4 (Fig. 1c) during fall and early winter, respectively. The seasonal conditions are evidently influential. In other words, thermal stratification was observed to be strong during the fall. The vertical temperature difference in the water surface within a depth of 3 m was approximately 1.5 °C. However, the temperature dropped drastically beyond 3 m (ΔT ≈4.5 °C) compared to the epilimnion temperature and averaged 18.25 °C. However, during early winter, the vertical difference between the temperature of the epilimnion and hypolimnion was approximately (ΔT ≈2.5 °C) and generally at an average of 11.5 °C.

Given that the mean air temperatures near the lake area (recorded on the same days when the lake temperature measurements were taken) were 18.86 °C and 9.9 °C, and the diurnal fluctuations of air temperature can also be considered as another controlling factor.

The strong thermal stratification in the fall compared to that in winter can be attributed to the strong solar radiation in the fall and the continuous exchange of heat flux on the water surface, enabling continuous energy accumulation in the lake (Yang et al., 2018). However, overcast weather coupled with strong winds that occur during winter creates some stirring and partial homogenization of the water in the lake. Moreover, penetrative

convection occurs more easily at night, resulting in a decrease in the lake water temperature and an additional degree of vertical mixing (Fig. 9b).

Fig. 9 Temperature profiles along water columns measured at P1, P2, P3, and P4, during (a) fall and (b) early winter

4. Discussion

4.1.Hydrodynamics in light of hydroacoustics measurements

The fundamental difference between a river and a lake is that the flow velocity of a lake is far weaker and is not driven by gravity. In addition, the dynamic processes in a dam lake are diverse and differ from those in rivers.

As demonstrated in this study, the travel-time principle is the backbone of the tomographic measurements obtained using the FAT system. Reciprocal acoustic pulses were triggered from both transducers concurrently, and the arrival times were determined from the cross-correlation patterns. Accordingly, the velocity and discharge were estimated using Eqs. (3) and (4), respectively.

The basic approach toward selecting the arrival times for upstream and downstream stations is to select the greatest arrival peak for each correlation pattern (Chen et al. 2018). However, Al Sawaf et al. (2020) found that found that implementing this approach is imprecise. In this study, we observed certain periods of single arrival peaks and others of double or multiple arrival peaks, where the largest arrival peak was observed in the second group, as demonstrated in Figs. 4a, 4b, 5a, and 5b.

Two interesting concerns emerged from these results. The first concern is regarding the certain periods showing only a single arrival peak, while other periods showing double or multiple arrival peaks. The second concern is with respect to determining the arrival peak to be selected for calculating the mean cross-sectional velocity when multiple arrival peaks instead of a single peak, is encountered. With respect to the first concern, the sound propagation of acoustic signals in shallow water environments is affected by several factors, including bed material, bathymetry shape, presence of composite layer stratifications of salinity, and different temperature layers (Nguyen et al., 2009; Thorne, 1998). The main hindrance for hydroacoustics experts is determining the exact path of each triggered signal from a transmitter to receiver along the acoustic path because of the above-mentioned features that control sound propagation in water. However, a simulation for sound ray propagation along the transmission line can illustrate the behavior of a transmitted acoustic ray in water. To accomplish this task, we used the method proposed by Dushaw (1998) for acoustic ray simulation:

$$\frac{d\beta}{dr} = \frac{\partial c}{\partial r}\frac{1}{c}\tan\beta - \frac{\partial c}{\partial z}\frac{1}{c} \qquad (10a)$$

$$\frac{dz}{dr} = \tan\beta \qquad (10b)$$

$$\frac{dt}{dr} = \frac{1}{c}\,\mathrm{Sec}\,\beta \qquad (10c)$$

where β is the angle of the sound ray estimated from the horizontal and vertical axes, i.e., *r* and *z,* respectively; *c* is sound speed; and *t* is the time.

Ray simulations were performed for water temperature measurements collected during early winter, as depicted in Fig. 9b. Figure 9b reveals that the temperature difference between the epilimnion and hypolimnion can be estimated as 2.5 °C. In other words, the sound speed at the bottom levels dropped by at least 10 m/s from the upper layers, as shown in Fig. 10. The speed of sound in the water was computed using Eq. (11) proposed by (Medwin 1975) as a function of water depth D (m) and temperature T (°C), whereas in fresh water, the salinity (S) term was insignificant.

$$c = 1449.2 + 4.6T - 0.055T^2 + 2.9 \times 10^{-4} T^3 + (1.34 - 0.01T)(S - 35) + 0.016D \quad (11)$$

Fig. 10 Ray simulated patterns along cross-sections of (a) S1_S2 and (b) T1_T2

Figure 10 and Table 3 present some interesting results. Along the transmission line S1_S2, two arrival groups can be identified; the difference between the first arrival peak and the second arrival peak was 0.27 ms, which is consistent with our observations. Likewise, three arrival groups can be observed along T1_T2. The time difference between the first arrival peak and the second arrival peak was 0.78 ms, which is also consistent with our recorded signals.

Table 3. Results of ray simulation along S1_S2 and T1_T2

Transmission line: S1_S2			
Group number	Ray length (m)	Arrival time (ms)	Difference with the first arrival time (ms)

Group I (Black)	253.82	173.74	0
Group II (Red)	254.18	174.03	0.29
Transmission line: T1_T2			
Group I (Black)	288.42	197.65	0
Group II (Red)	289.80	198.43	0.78

446

447 The thermal stratification of the lake indicates that even in the case of relatively low
448 temperature differences between the epilimnion and hypolimnion during winter, as shown
449 in Fig. 9b, the cold temperature of the hypolimnion acts as a shield that obstructs and
450 weaken sound from reaching the warmer layers of the epilimnion for obtaining the largest
451 peak clearly as shown in Fig. 10. Figure 3b also shows that, remarkably, when water
452 release reached 15 m^3/s, the water temperature in the lake did not decrease rapidly. This
453 suggests that water release at this rate neither yields a notable feature nor causes apparent
454 thermal mixing.

455 To holistically elucidate the observed arrival groups along the two transmission lines with
456 respect to different water temperatures, the arrival times were estimated using the sound
457 speed values. The corresponding arrival times can be calculated by substituting the water
458 temperature readings obtained by the CTD (Fig. 9b) into Eq. (11). Hence, sound speeds
459 at –1 m and □3.8 m were 1456.35 m/s and 1448.90 m/s, respectively; the arrival times
460 are presented in Table 4. Notably, the calculated arrival times are comparable to the

461 simulated values listed in Table 3. Hence, the effect of different temperature layers on
462 generating multi-arrival peaks is elucidated.

463 **Table 4.** Arrival times estimated using Eq. (10) along two different temperature layers

Depth (m)	Temperature (℃)	Sound speed (m/s)	Arrival time (ms) = $\frac{Tranmission\ Length\ (m)}{Sound\ Speed\ (m/s)} * 1000$	
			S1_S2	T1_T2
–1.00	12.57	1456.42	173.7	197.40
–3.80	10.63	1449.11	174.6	198.4

464

465 The second concern emerges from these findings: which arrival peak should be selected
466 for the estimation of water velocity and discharge when multiple (instead of single) arrival
467 peaks are encountered (the first or delayed arrival peak)? Initially, various arrival time
468 groups were observed along S1_S2 and T1_T2. Nevertheless, in most cases, the received
469 signals from the cross-correlation patterns only showed one apparent single peak located
470 within the range of the first group, and some of the recorded signals showed double or
471 multiple peaks, where one peak appeared within the range of the first group (i.e., peaks
472 located along the red and blue peaks shown in Figs. 4a, 4b, 5a, and 5b), and the largest
473 peak arrived later. Therefore, we presumed the first peak to be desirable and not
474 necessarily the largest one. However, for a concrete demonstration, we estimated the
475 mean cross-sectional water temperature using the FAT system along T1_T2. In this
476 scenario, we used the arrival times of the first and delayed arrival peaks to estimate the
477 mean water temperature and then, compared the results to the temperature records
478 obtained by the water level-temperature logger, as shown in Fig. 11.

The different arrival time groups observed along T1_T2 in Fig. 11a were used to estimate the sound speed using Eq. (12), and the mean water temperature along the transmission line was determined by substituting the sound speed obtained by the FAT in Eq. (11).

$$c = \frac{R_i}{2} \times \left(\frac{1}{t_{T1}} + \frac{1}{t_{T2}}\right) \quad (12)$$

where R_i is the ray length obtained from the ray simulation in Table 3 (i.e., R_1 = 288.42 m and R_2 = 288.9 m) because ray length is a function of water temperature and bathymetry shape.

The trivial difference (i.e., 1 ms) between the first and delayed arrivals, as shown in Fig. 11a, resulted in a temperature difference estimated to be approximately 0.5 °C, which is sizeable (see Fig. 11b); therefore, our assumption with respect to using the first arrival peak appears to be valid.

Fig. 11 a) Sample of arrival times with first and delayed arrival peaks and b) time-series for mean water temperature estimated by FAT at 30 kHz (red) compared to mean water obtained by water level-temperature logger (black)

4.2. Internal waves

One of the novel findings of this monitoring program was the ability to detect internal seiches using a crossed acoustic path scheme (Fig. 8a). To illustrate this, Fig. 8a shows the temporal variations in the flow direction; however, the flow mainly fluctuated between the first and second quadrants (Q1 and Q2) over a period of approximately 3 h. This phenomenon can be attributed to internal seiches in the lake and may have caused the difference between the densities of the epilimnion and hypolimnion as a result of

501 inflow pulses into the lake. Mortimer (1952) stated that if exposing a stratified lake with
502 different densities at the epilimnion, ρ_e, and hypolimnion, ρ_h, to a steady wind, the
503 surface water moves toward the leeward bank due to frictional drag and wave action. The
504 wind generates a slope on the lake surface uphill in the same direction as the wind,
505 causing a return flow in the lower part of the epilimnion. Simultaneously, a sizable tilt
506 forms at the interface opposite to the surface tilt; this is accompanied by a thermocline
507 slope. In a two-layer stratified lake, the period (P) of the seiche can be estimated as
508 follows:

509 $$P = \frac{2 \times L}{\sqrt{g \times \{(\rho_h - \rho_e)/(\frac{\rho_h}{h_h} + \frac{\rho_e}{h_e})\}}} \qquad (13)$$

510 where L is the length of the water body; g is the acceleration of gravity; and h_e and h_h are
511 the average thicknesses of the epilimnion and hypolimnion layers, respectively. Upon
512 substituting the average density values of the epilimnion and hypolimnion obtained from
513 the CTD, the internal wave period was calculated to be 3 h, which confirms our
514 assumptions.

515 *4.3.Performance of inflow acquired by fluvial acoustic tomography (FAT) system*

516 To verify the performance of the inflow acquired by FAT (Q_{FAT}), four transects were
517 conducted as another independent technique along the direct line between the right and
518 left banks at points (R) and (L) using a Teledyne RDI Workhorse Monitor ADCP (Q_{ADCP})
519 operating at 1228.8 kHz, as shown in Fig. 1c. The data obtained via the Q_{ADCP} appear to
520 be comparable to those obtained via Q_{FAT} and Q_{HDMO}, as shown in Fig. 12a. The difference
521 among the three methods (Q_{FAT}, Q_{HDMO}, and Q_{ADCP}) is not very significant, considering

522 we worked with considerably slow velocities. Hence, the velocity, to the best of our
523 knowledge, was within the limit of most velocity-measuring instruments. The velocity
524 resolution of the acoustic doppler current profiler (ADCP) can be made reliable by
525 averaging a large set of ping data. Unfortunately, we were unable to use a bottom-fixed
526 ADCP because the dam lake was utilized by certain local fishermen. In addition,
527 deploying a fixed ADCP above the accumulated sediments in the center of the lake was
528 unsafe.

529 In the absence of a reliable inflow monitoring method, we cannot accurately verify the
530 ultimate performance of the FAT system. Figure 12b reveals a type of low resolution
531 associated with dam inflow records obtained by the HDMO, compared with the measured
532 stage. Therefore, the monotonous inflow behavior can be understood by observations
533 made using the HDMO.

534 **Fig. 12** a) Comparison between inflow acquired by fluvial acoustic tomography (FAT;
535 black), Haji Dam Monitoring Office (HDMO; red), acoustic doppler current profiler
536 (ADCP; green), and outflow by HDMO (blue), and b) association between stage and
537 inflow as recorded by HDMO

538

539 *4.4.Comparison with previous studies and scope for future research*

540 Most of the previous monitoring applications via the FAT system were accomplished
541 using a 30 kHz transmission frequency. However, the 30-kHz system has a certain range
542 of transmission length between a pair of transducers, and the minimum water depth must
543 exceed ~0.5 m for effective use (Razaz et al. 2015). Consequently, in 2016, the first
544 version of the FAT system that can be operated using 53 kHz frequency was developed

for use in relatively shallower and narrower streams, with higher velocity resolution. Bahreinimotlagh et al. (2016) performed the first discharge monitoring via a cross-transmission configuration using one pair of 30-kHz systems and another of 53-kHz systems in a mountainous river. Their findings confirmed that the velocity resolution was augmented twice when using 53 kHz, with a minimum recorded value of 0.2 m/s. Recently, (Al Sawaf et al. 2020) successfully acquired accurate river velocity for very shallow conditions using a 53-kHz system. The minimum acquired velocity was 0.1 m/s (obtained for a cross-section), with a minimum depth of 28 cm.

In the current observation, two different frequencies were used in a very slow flow condition. Figures 6 and 7 demonstrate that the current velocities captured at 53 kHz seem to be more precise than those obtained at 30 kHz, with a mean absolute cross-sectional velocity of 1.5 cm/s, which is a significant accomplishment.

The precision of the hydroacoustic measurements depends substantially on determining the exact arrival time, and even a mistake as tiny as a sub-millisecond can generate enormous errors. Hence, the FAT system can provide reliable measurements even in extremely slow water-velocity environments. As seen in Fig. 11, the delayed arrival times resulted in increased temperatures compared to the first arrival times.

Another interesting feature in this study is that we improved the flow direction approach proposed by Bahreinimotlagh et al. (2016) for use in different situations. Our improved approach is flexible and appropriate for determining the flow direction not only in cases of dam inflow but also in various circumstances, such as tidal rivers (wherein the flow shifts from landward to seaward and vice versa), and can clarify the occurrence of

567 negative inflow periods. However, we used the temporal variations of the ensemble
568 inflow direction because we assumed that the reservoir inflow direction would not vary
569 significantly over a short period.

570 Although some of our findings are preliminary, our results are encouraging. The FAT
571 system is capable of capturing flow direction and water velocity; therefore, future studies
572 should consider longer periods to determine the linkage between a fluctuating inflow,
573 while maximizing power generation capacity.

574 Moreover, future studies should examine the hysteresis relationship of the variation in the
575 water flow direction during the opening and closing of the dam gate. Additionally, the
576 relationship between flow direction and inflow velocity can be used to propose another
577 superior equation to supplement the traditional water balance equation because this
578 information captures the velocity along the flow direction in the entire cross-section
579 rather than in a small portion (H-ADCP).

580 Finally, future research should utilize the findings of this study to improve existing
581 analytical models and seek the most accurate inflow quantities using the travel-time
582 principle of underwater acoustics.

583 **5. Conclusions**

584 The ability to acquire reliable real-time and continuous records of flow data can facilitate
585 optimal utilization of water resources, elucidate hydrologic information, and allow for
586 optimal ecological and societal outcomes. In this study, we observed the water inflow to
587 a dam lake using the FAT system, based on the travel-time approach. The main goal of
588 this study is to offer a practical and reliable monitoring approach for understanding the

589 inflow to a lake, investigating the behavior of underwater acoustic communications
590 within very slow flow environments, and analyzing the related hydrological processes.
591 Two pairs of FAT systems were placed diagonally upstream of a dam lake at two different
592 frequencies. We upgraded the flow direction estimation based on travel-time behavior.
593 Additionally, we discussed the importance of using accurate tomographic data in inflow
594 monitoring and demonstrated that a small mistake in tomographic records (even by a sub-
595 millisecond) could generate substantial errors.

596 Generally, inflow monitoring based on the travel-time approach appears to be practical
597 and can be considered as a promising and competitive application. In this study, the flow
598 direction was continuously deduced via reciprocal sound transmission using a cross-
599 configuration transmission, and the flow direction equation was improved for
600 applicability to a fluctuating water flow environment. However, the precision of the
601 values is a function of velocity resolution. Our findings reveal that the smallest mistake
602 in selecting the exact arrival times (even by a sub-millisecond) can generate a substantial
603 error. Hence, the FAT system can yield reliable measurements. An interesting study
604 finding is the ability of the FAT system to detect the presence of internal waves (i.e.,
605 seiches) based on the travel-time approach and upgraded flow direction equation.

606 **Declarations**

607 **Acknowledgments**

608 The authors are grateful to the Haji Dam Monitoring Office, Hiroshima, Japan for the
609 data they shared.

610 **Funding**

611 This study was funded by the Electric Technology Research Foundation of Chugoku,
612 Japan.

613 **Compliance with Ethical Standards**

614 **Competing Interests**: The authors declare that they have no conflicts of interest.

615 **Availability of data and materials**

616 Streamflow data computed by Q_{HDMO} were provided by the Haji Dam Monitoring Office,
617 Hiroshima, Japan. The Q_{FAT} observations determined in this study can be accessed from
618 the corresponding author upon request.

619 **Consent to Participate**: Not applicable.

620 **Consent to Publish**: Not applicable.

621 **Ethical Approval:** Not applicable.

622 **Author contribution:**

623 **Mohamad Basel Al Sawaf:** Conceptualization, methodology, software, data curation,
624 and writing - original draft preparation.

625 **Kiyosi Kawanisi**: Supervision, conceptualization, methodology, validation, reviewing
626 and editing, validation, and original draft revision.

627 **Cong Xiao**: Reviewing and editing, validation, and discussion.

628 **Gillang Noor Nugrahaning Gusti:** Data curation and validation.

629 **Faruq Khadami:** Data curation and validation.

630

631 **References**

632 Ahmad SK, Hossain F (2019) A generic data-driven technique for forecasting of
633 reservoir inflow: Application for hydropower maximization. Environ Model Softw
634 119:147–165. https://doi.org/10.1016/j.envsoft.2019.06.008

635 Al Sawaf MB, Kawanisi K, Xiao C (2020) Measuring Low Flowrates of a Shallow
636 Mountainous River Within Restricted Site Conditions and the Characteristics of
637 Acoustic Arrival Times Within Low Flows. Water Resour Manag 34:3059–3078.
638 https://doi.org/10.1007/s11269-020-02557-w

639 Allan JD (2004) Landscapes and Riverscapes: The Influence of Land Use on Stream
640 Ecosystems. Annu Rev Ecol Evol Syst 35:257–284.
641 https://doi.org/10.1146/annurev.ecolsys.35.120202.110122

642 Bahreinimotlagh M, Kawanisi K, Danial MM, et al (2016) Application of shallow-water
643 acoustic tomography to measure flow direction and river discharge. Flow Meas
644 Instrum 51:30–39. https://doi.org/10.1016/j.flowmeasinst.2016.08.010

645 Brian D Dushaw JAC (1998) Ray Tracing for Ocean Acoustic Tomography

646 Budu K (2014) Comparison of Wavelet-Based ANN and Regression Models for
647 Reservoir Inflow Forecasting. J Hydrol Eng 19:1385–1400.
648 https://doi.org/10.1061/(ASCE)HE.1943-5584.0000892

649 Chen M, Syamsudin F, Kaneko A, et al (2018) Real-Time Offshore Coastal Acoustic
650 Tomography Enabled With Mirror-Transpond Functionality. IEEE J Ocean Eng.
651 https://doi.org/10.1109/JOE.2018.2878260

652 Deng C, Liu P, Guo S, et al (2015) Estimation of nonfluctuating reservoir inflow from
653 water level observations using methods based on flow continuity. J Hydrol
654 529:1198–1210. https://doi.org/10.1016/j.jhydrol.2015.09.037

655 Gupta H, Kao S-J, Dai M (2012) The role of mega dams in reducing sediment fluxes: A
656 case study of large Asian rivers. J Hydrol 464–465:447–458.
657 https://doi.org/10.1016/j.jhydrol.2012.07.038

658 Hadiyan PP, Moeini R, Ehsanzadeh E (2020) Application of static and dynamic
659 artificial neural networks for forecasting inflow discharges, case study: Sefidroud
660 Dam reservoir. Sustain Comput Informatics Syst 27:100401.
661 https://doi.org/10.1016/j.suscom.2020.100401

662 Hariri-Ardebili MA (2018) Risk, Reliability, Resilience (R3) and beyond in dam
663 engineering: A state-of-the-art review. Int J Disaster Risk Reduct 31:.
664 https://doi.org/10.1016/j.ijdrr.2018.07.024

665 Kawanisi K, Razaz M, Ishikawa K, et al (2012) Continuous measurements of flow rate
666 in a shallow gravel-bed river by a new acoustic system. Water Resour Res 48:1–
667 10. https://doi.org/10.1029/2012WR012064

668 Medwin H (1975) Speed of sound in water: A simple equation for realistic parameters. J
669 Acoust Soc Am 58:1318–1319. https://doi.org/10.1121/1.380790

670 Mortimer CH (1952) Water movements in lakes during summer stratification; evidence
671 from the distribution of temperature in Windermere. Philos Trans R Soc Lond B
672 Biol Sci 236:. https://doi.org/10.1098/rstb.1952.0005

673 Nazeer S, Hashmi MZ, Malik RN (2016) Spatial and seasonal dynamics of fish
674 assemblage along river Soan, Pakistan and its relationship with environmental
675 conditions. Ecol Indic 69:780–791. https://doi.org/10.1016/j.ecolind.2016.05.034

676 Nguyen H, Kaneko A, Lin J, et al (2009) Acoustic Measurement of Multisubtidal
677 Internal Modes Generated in Hiroshima Bay, Japan. IEEE J Ocean Eng 34:103–
678 112. https://doi.org/10.1109/JOE.2009.2014933

679 Razaz M, Kawanisi K, Kaneko A, Nistor I (2015) Application of acoustic tomography
680 to reconstruct the horizontal flow velocity field in a shallow river. Water Resour
681 Res 51:9665–9678. https://doi.org/10.1002/2015WR017102

682 Simon MK, Omura JK LB (1985) Spread Spectrum Communications Handbook.
683 McGraw-Hill:, New York, 423

684 Stähly S, Franca MJ, Robinson CT, Schleiss AJ (2019) Sediment replenishment
685 combined with an artificial flood improves river habitats downstream of a dam. Sci
686 Rep 9:5176. https://doi.org/10.1038/s41598-019-41575-6

687 Suzuki H, Ochiai A, Kuda M, Mizoguchi A (2008) Investigation about Accuracy of
688 Discharge Data Controlled by Multi-Reservoir System on Jinzu River Using
689 Inflow Estimation Method Based on Digital Filter. J JAPAN Soc Hydrol WATER
690 Resour 21:285–295. https://doi.org/10.3178/jjshwr.21.285

691 Tao T (1999) Local inflow calculator for reservoirs. Can Water Resour J 24:.
692 https://doi.org/10.4296/cwrj2401053

693 Thorne RE (1998) Review: Experiences with shallow water acoustics. Fish Res.

https://doi.org/10.1016/S0165-7836(98)00068-X

Zhu X-H, Zhang C, Wu Q, et al (2012) Measuring discharge in a river with tidal bores by use of the coastal acoustic tomography system. Estuar Coast Shelf Sci 104–105:54–65. https://doi.org/10.1016/j.ecss.2012.03.022

Figures

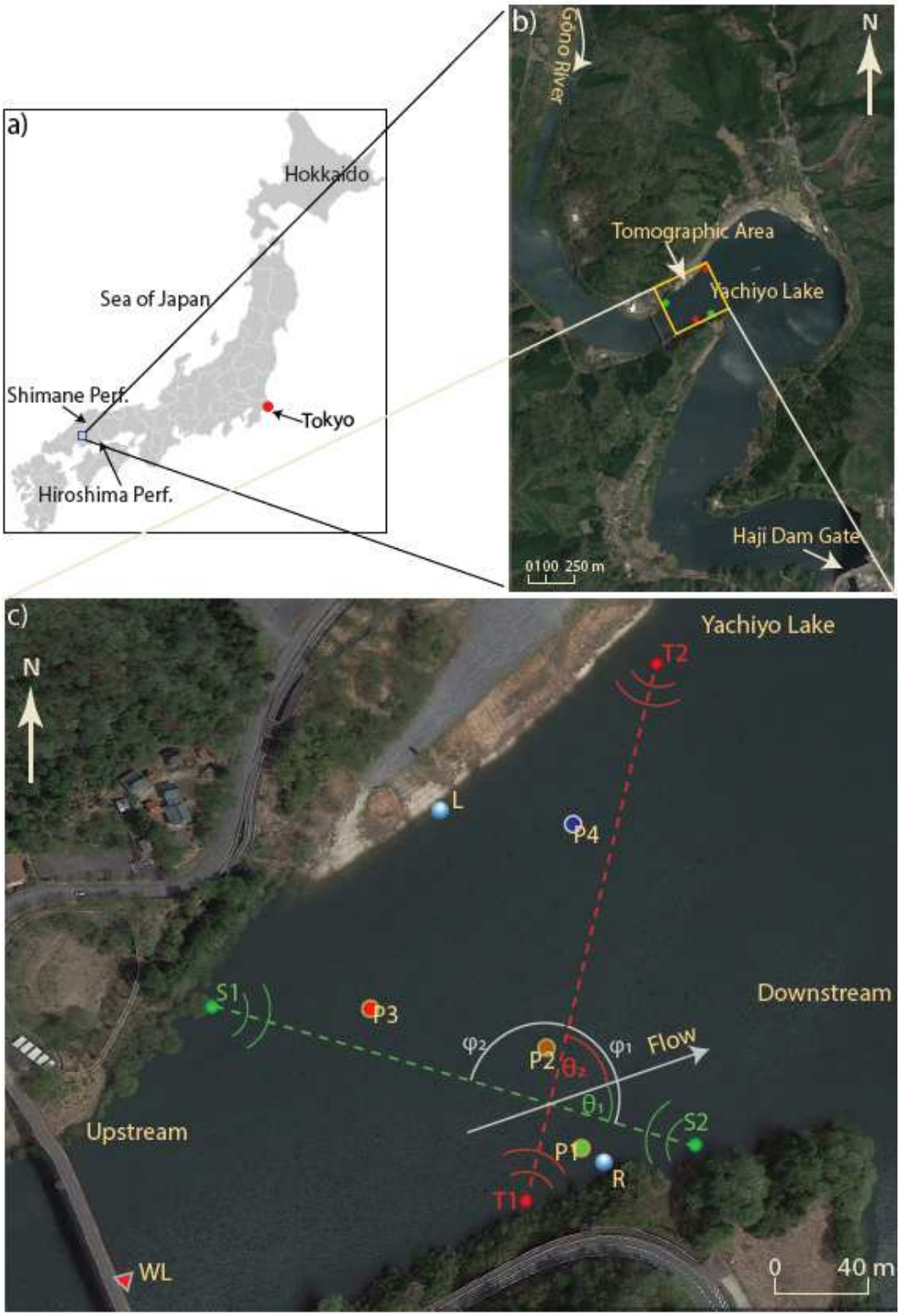

Figure 1

a) Location of the observation site; b) map showing Gōno River, Haji Dam, and Yachiyo Lake; and c) study area map with inflow measurement zone and instrument positions Note: The designations employed and the presentation of the material on this map do not imply the expression of any opinion

whatsoever on the part of Research Square concerning the legal status of any country, territory, city or area or of its authorities, or concerning the delimitation of its frontiers or boundaries. This map has been provided by the authors.

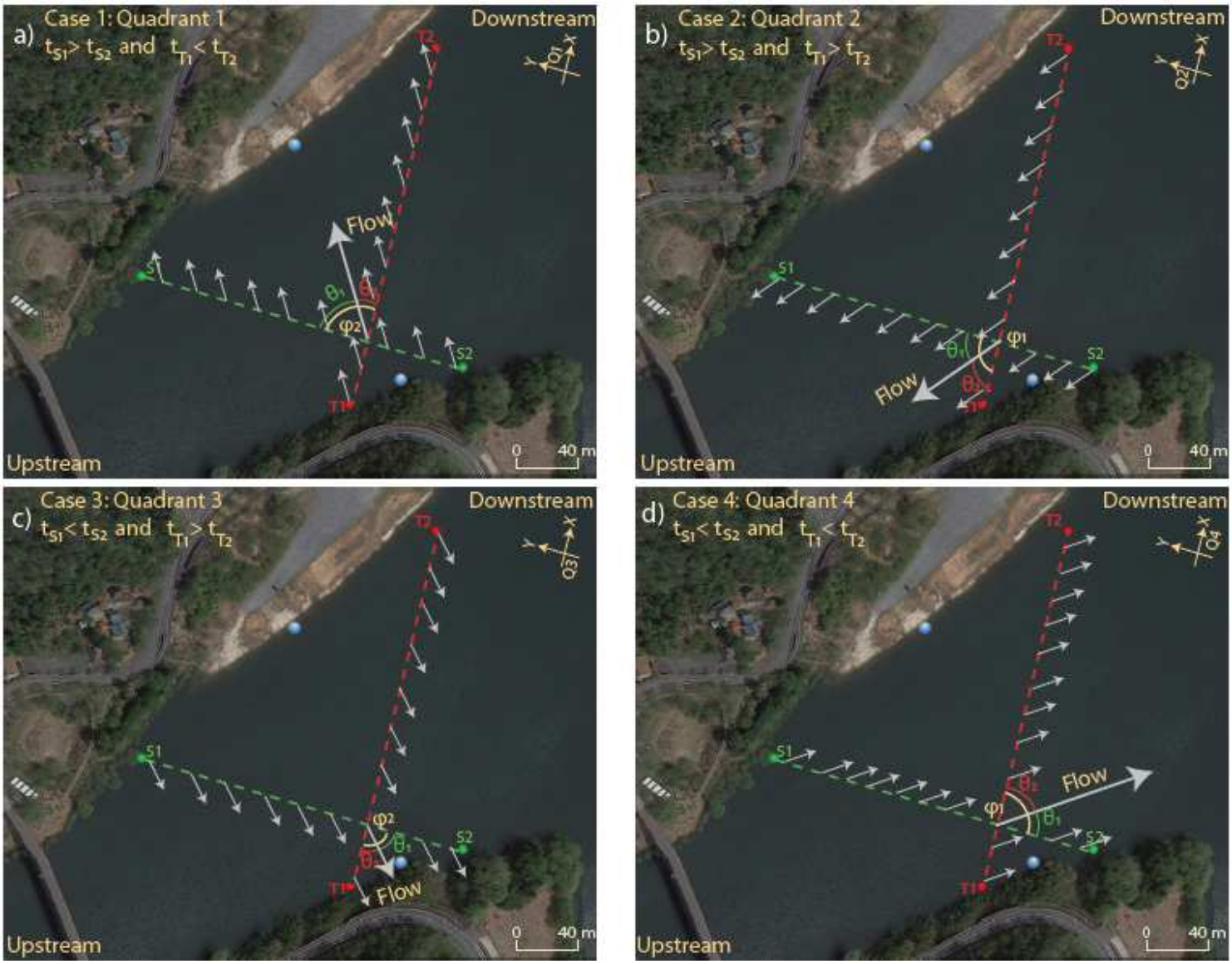

Figure 2

Visualization of flow direction over proposed axes according to recorded arrival times

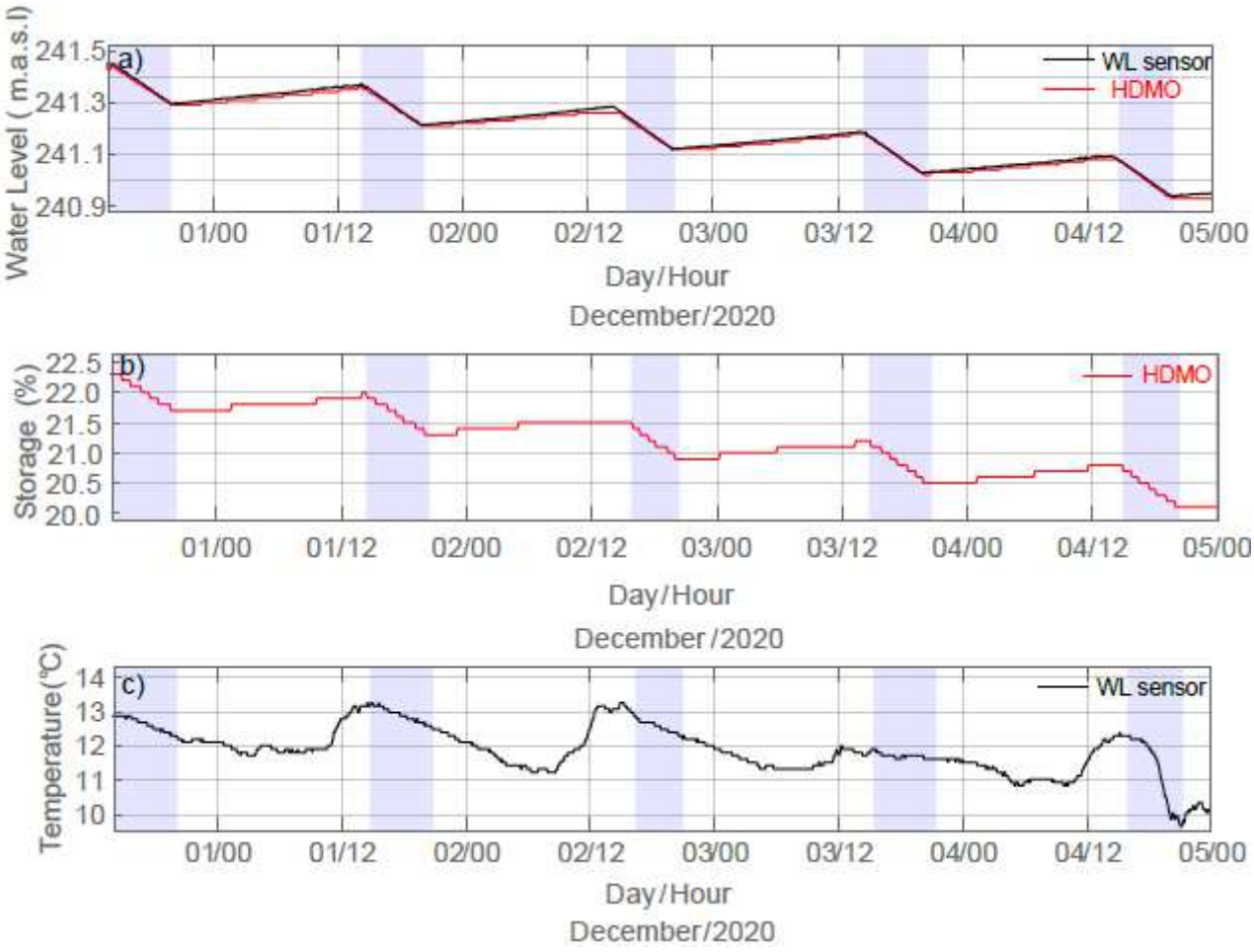

Figure 3

Time series plots of a) mean water level recorded by Haji Dam Monitoring Office (HDMO; red) and water level-temperature sensor (black), b) temporal variation of storage, and c) average water temperature. Releasing periods are shaded in blue

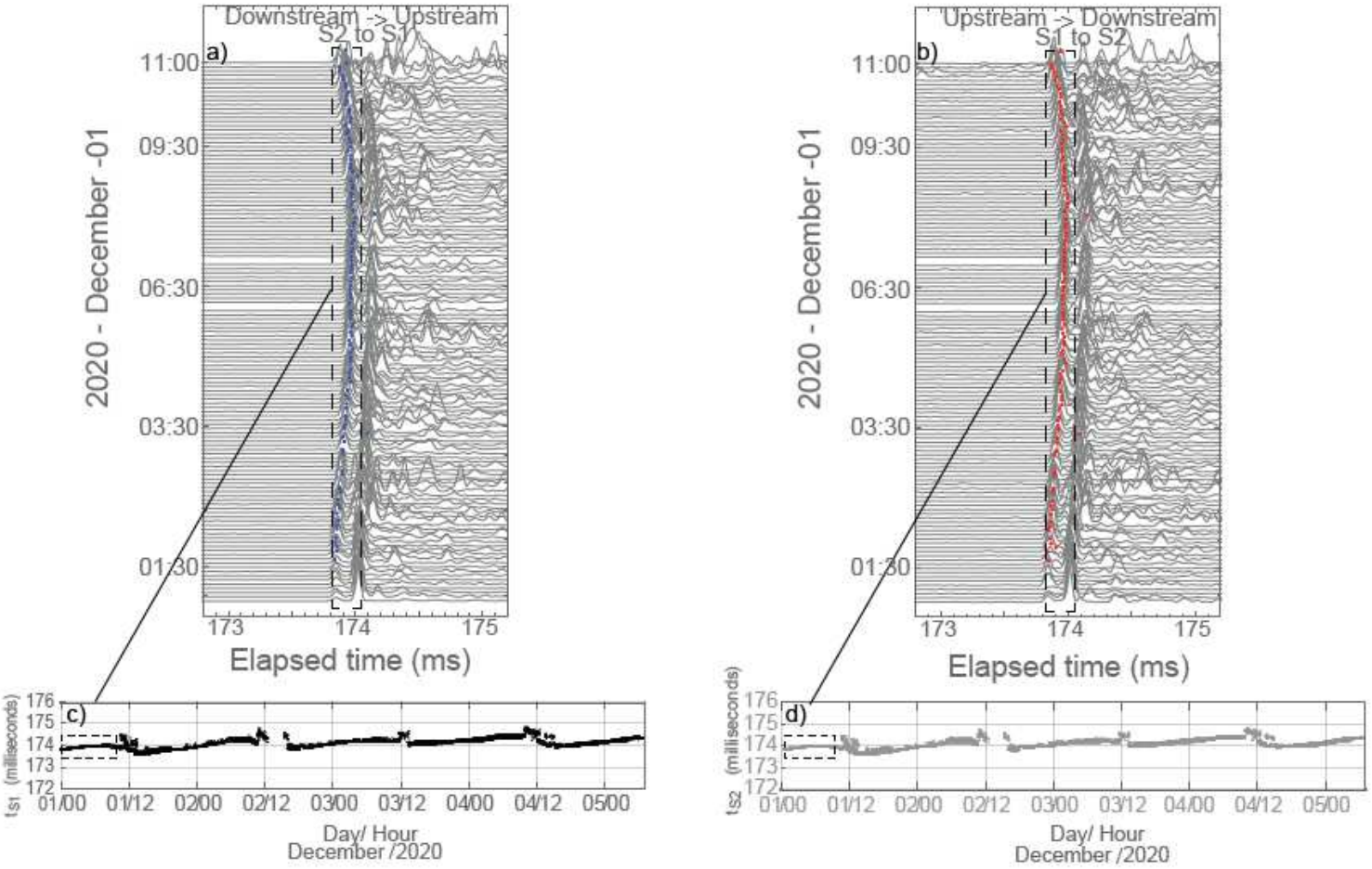

Figure 4

Arrival time records of 53-kHz system: sample of stack diagram of correlated signals recorded on December 1, 2020, with a 5-min interval, (a) blue dots are the selected peaks of the arrival times downstream and (b) red dots are the selected peaks of the arrival times upstream. Time series plots of arrival times (in ms) obtained by (c) the downstream (black) and (d) upstream (gray) transducers

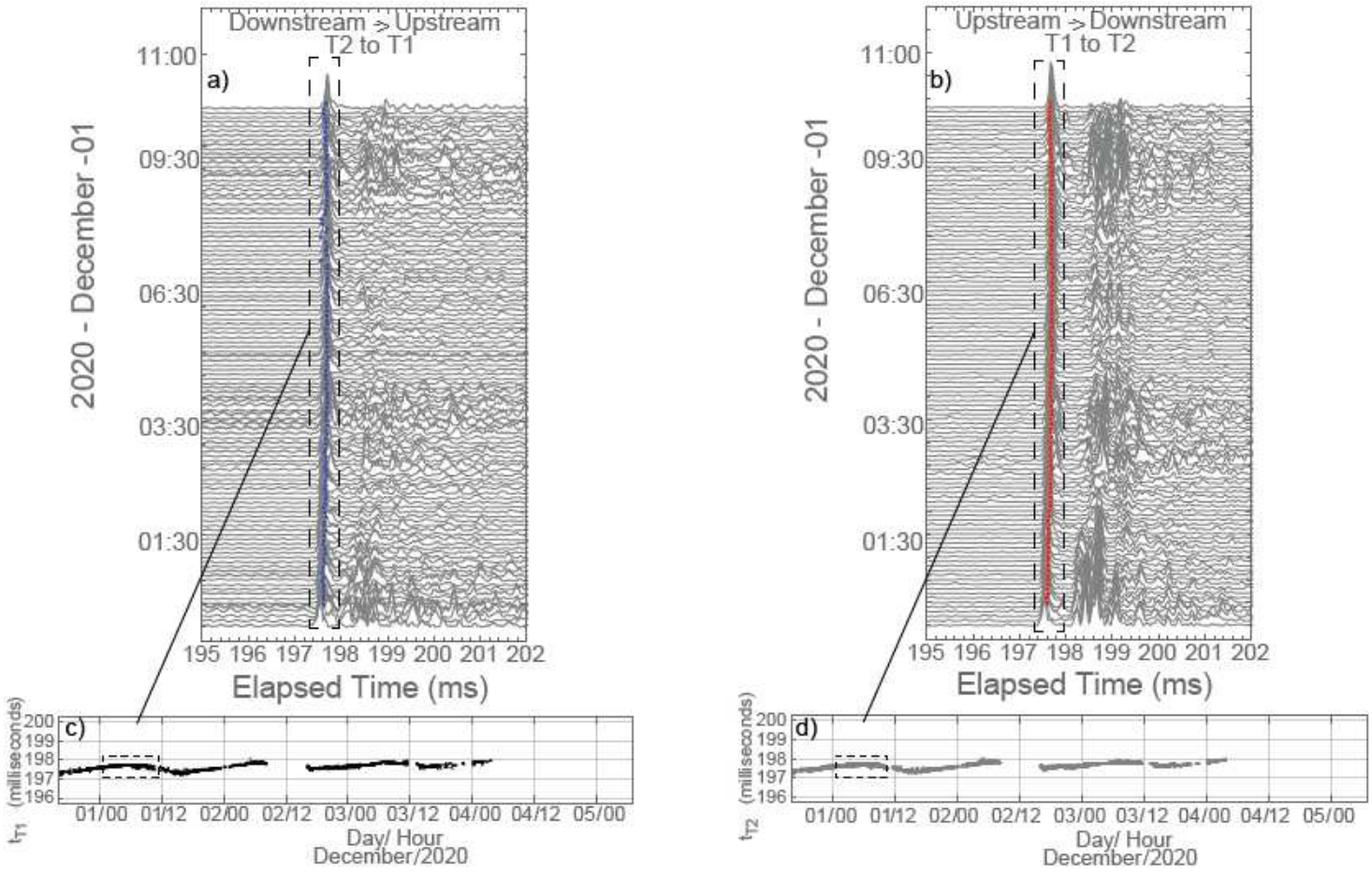

Figure 5

Arrival time records of 30-kHz system: sample of stack diagram of correlated signals recorded on December 1, 2020, with a 5-min interval, (a) blue dots represent selected peaks of arrival times downstream, and (b) red dots represent selected peaks of arrival times upstream. Time series plots of arrival times (in ms) obtained by (c) downstream (black) and (d) upstream (gray) transducers

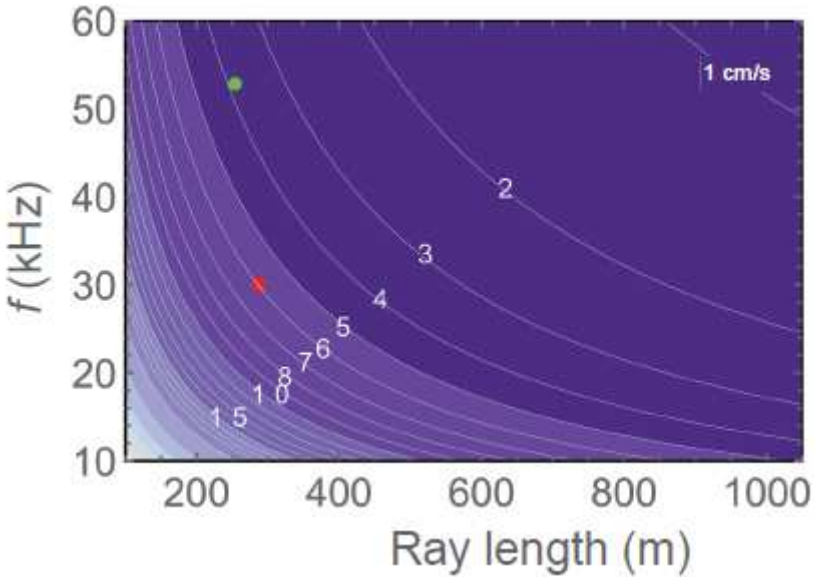

Figure 6

Velocity resolution of fluvial acoustic tomography (FAT) as a function of acoustic ray length and transducer frequency; green and red dots denote velocity resolution in accordance with distance and frequency for S1_S2 and T1_T2, respectively

Figure 7

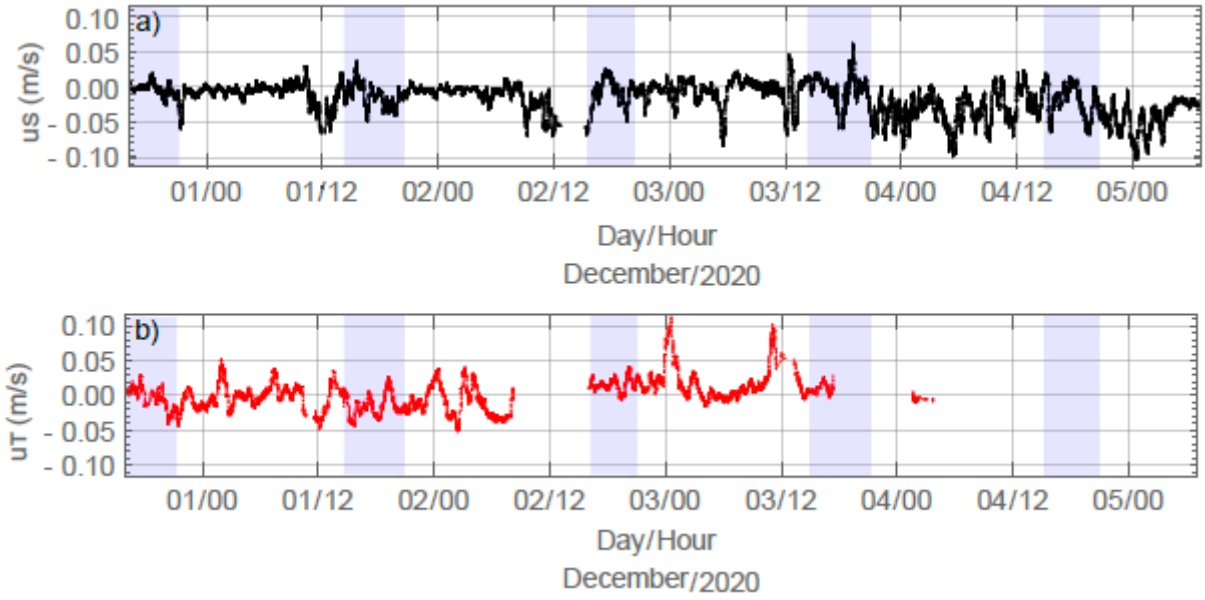

Mean average velocity along transmission lines: (a) S1_S2 (black), and (b) T1_T2 (red). Releasing periods are highlighted in blue

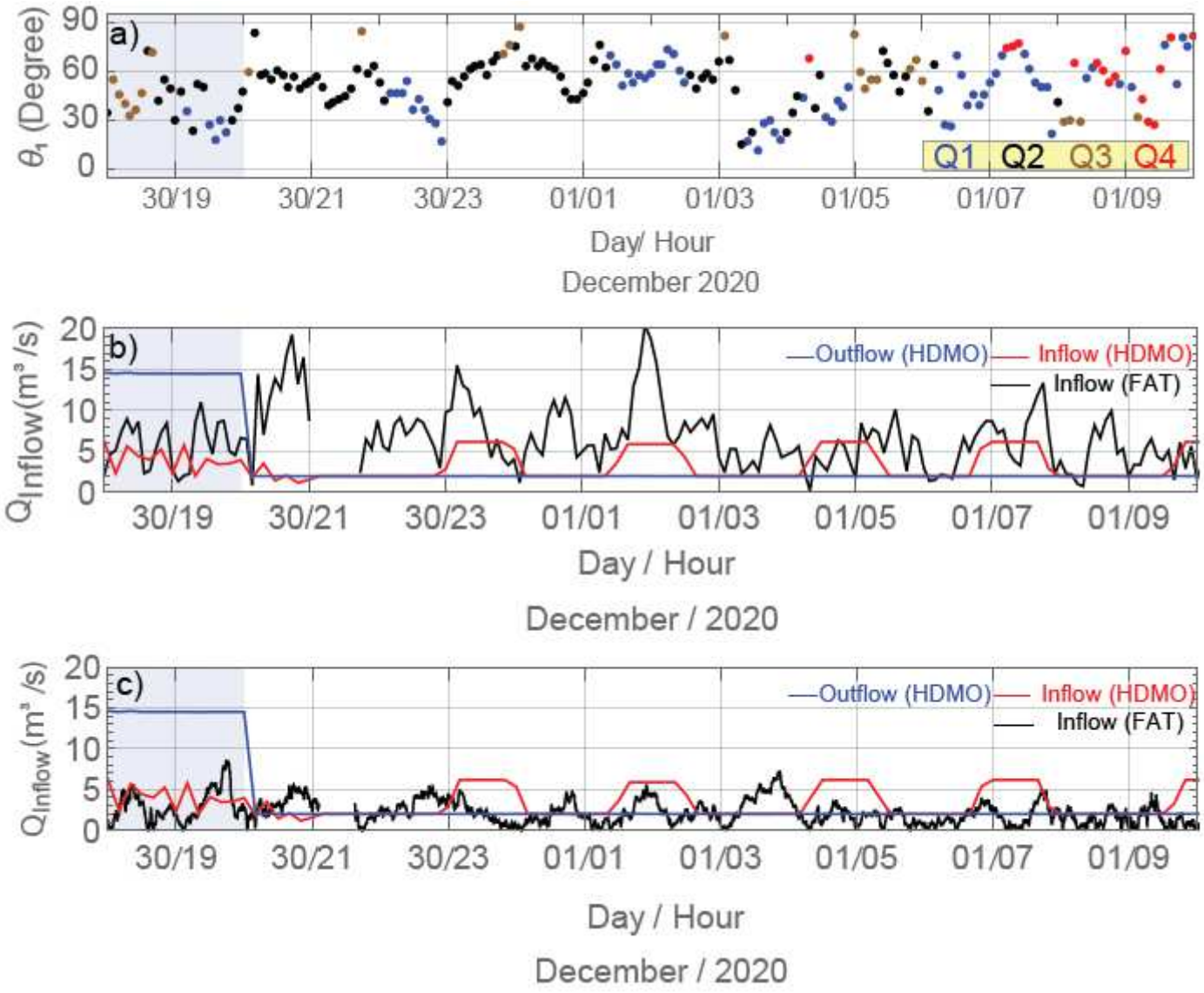

Figure 8

Time series plots of a) water flow (inflow) direction according to its corresponding quadrant, b) inflow estimated by fluvial acoustic tomography (FAT) (black) and by HDMO (red), and outflow acquired by Haji Dam Monitoring Office (HDMO; blue), and c) inflow by acquired by FAT using the mean flow direction θ = 21.47° (black) and by HDMO (red), and outflow by HDMO (blue); Releasing period is highlighted in blue

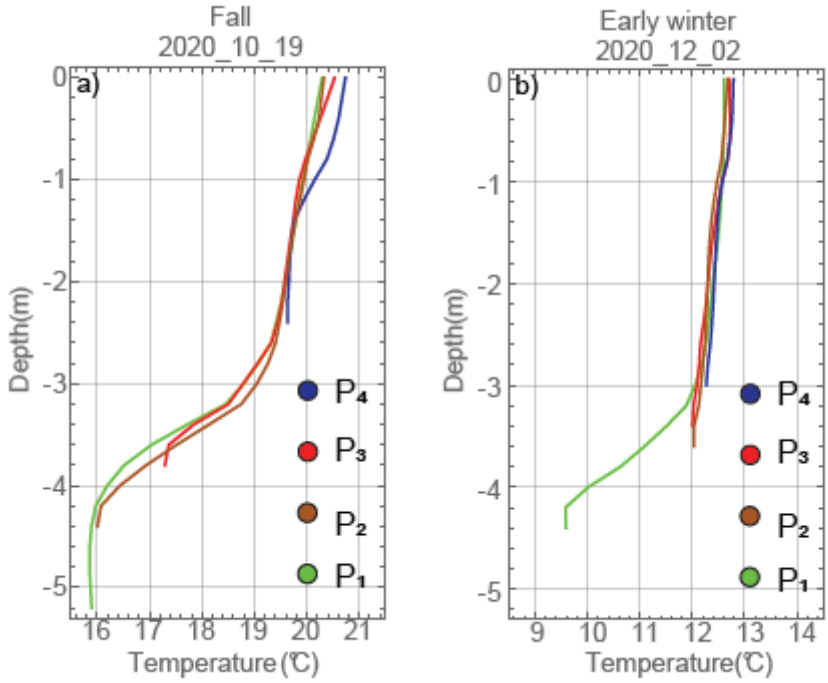

Figure 9

Temperature profiles along water columns measured at P1, P2, P3, and P4, during (a) fall and (b) early winter

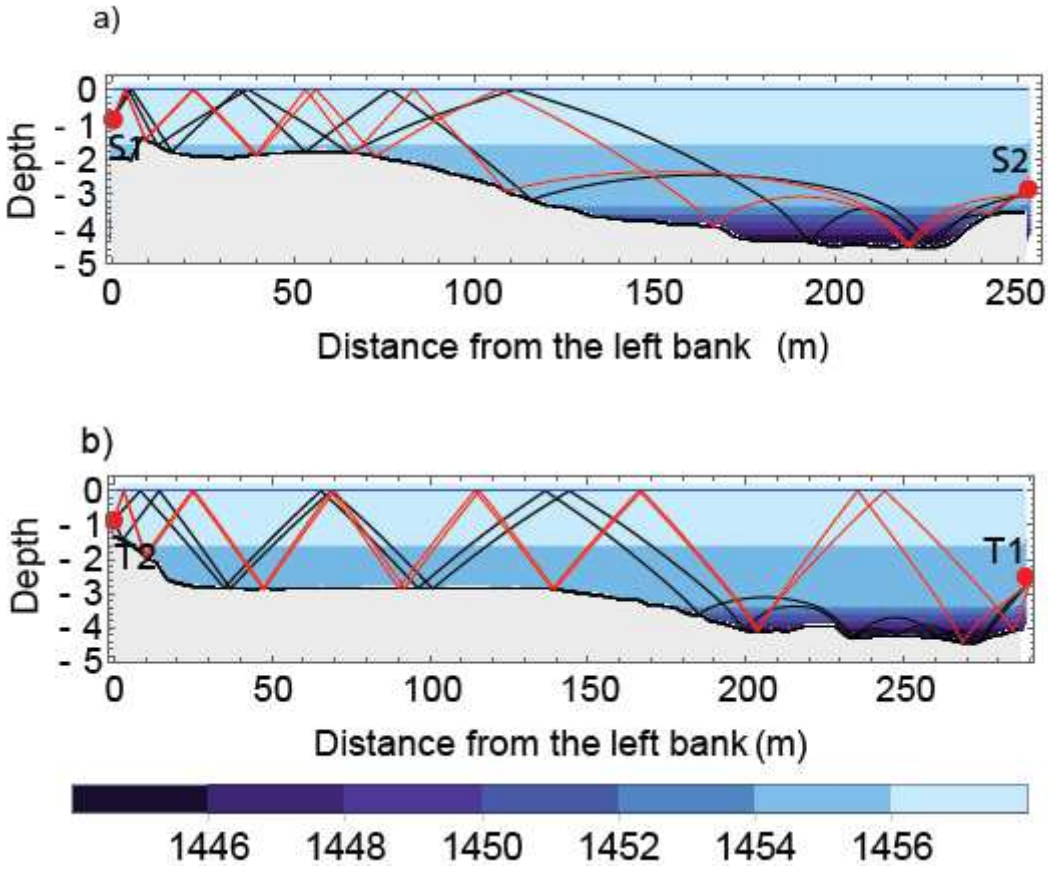

Figure 10

Ray simulated patterns along cross-sections of (a) S1_S2 and (b) T1_T2

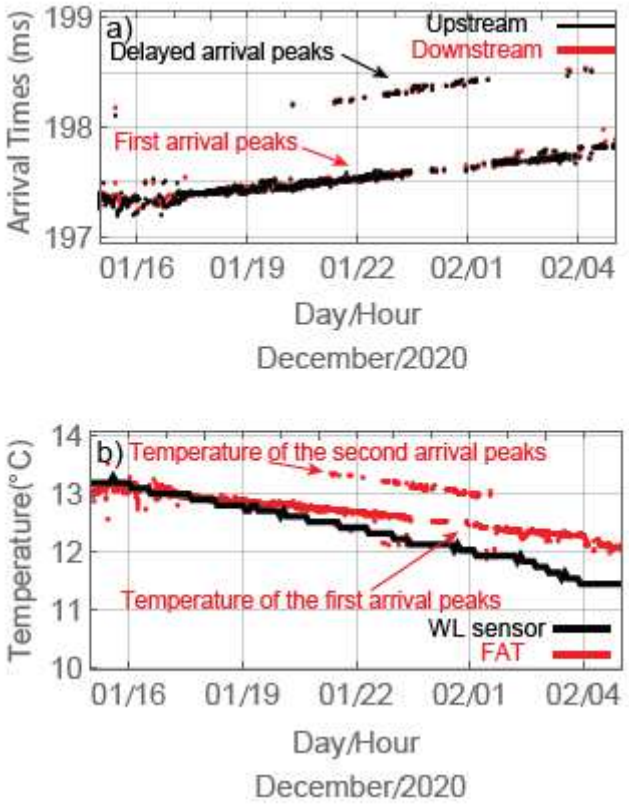

Figure 11

a) Sample of arrival times with first and delayed arrival peaks and b) time-series for mean water temperature estimated by FAT at 30 kHz (red) compared to mean water obtained by water level-temperature logger (black)

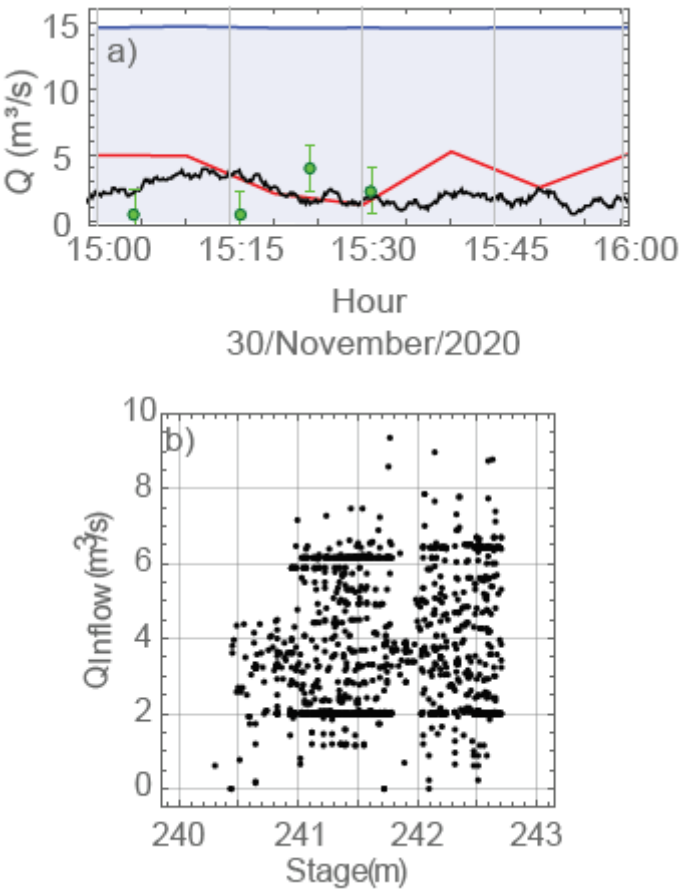

Figure 12

a) Comparison between inflow acquired by fluvial acoustic tomography (FAT; black), Haji Dam Monitoring Office (HDMO; red), acoustic doppler current profiler (ADCP; green), and outflow by HDMO (blue), and b) association between stage and inflow as recorded by HDMO